BEHAVIOUR AND DESIGN OF COLD-FORMED HIGH STRENGTH STEEL RHS T-JOINTS UNDERGOING COMPRESSION LOADS AT ELEVATED TEMPERATURES

Madhup Pandey[1] and Ben Young[2,*]

[1]*Department of Civil Engineering, University of Nottingham, Nottingham, United Kingdom.*
[2]*Department of Civil and Environmental Engineering, The Hong Kong Polytechnic University, Hong Kong, China.*

Abstract

This study presents a comprehensive numerical program aiming to investigate the static resistances of cold-formed high strength steel (CFHSS) T-joints with square and rectangular hollow section (SHS and RHS) braces and chords at elevated temperatures. The included angle between brace and chord members was 90°. The static behaviour of simply supported SHS and RHS T-joints undergoing compression loads through brace members was investigated at four elevated temperatures, including 400°C, 500°C, 600°C and 1000°C. The mechanical properties at elevated temperatures given in the literature for cold-formed S900 steel grade tubular members were used in this study. The numerical investigation was performed using the finite element (FE) models developed and validated by Pandey et al. [1] and Pandey and Young [2] for cold-formed S960 steel grade T-joints at ambient temperature and post-fire conditions. In total, 756 FE T-joint specimens were analysed in this numerical study, including 189 FE T-joint specimens for each elevated temperature. The tubular T-joint specimens were failed by chord face failure, chord side wall failure and a combination of these two failure modes. The resistances of investigated T-joints at elevated temperatures were compared with the nominal resistances predicted from design rules given in European code and CIDECT using the mechanical properties at elevated temperatures. Overall, it is shown that the current design rules given in European code and CIDECT are uneconomical and unreliable. As a result, economical and reliable design rules are proposed in this study through two design approaches for predicting the resistances of cold-formed steel SHS and RHS 90° T-joints of S900 grade at elevated temperatures.

Keywords: Cold-formed steel; Design equations; Elevated temperature; FE analysis; Tubular members; Welded joints.

*Corresponding author. (e-mail: ben.young@polyu.edu.hk).

1. Introduction

Tubular steel structures are subjected to different types of loading and also susceptible to extreme natural events, including fire. Adequate performance of joints under different adverse conditions is a prerequisite to ensure the integrity of the overall structure. Welded joints of a tubular steel structure need careful design considerations due to the presence of geometric discontinuity, stress concentration, complex failures, residual stresses and fabrication defects. It is an acknowledged fact that steel materials are quite sensitive to fire. The strength and stiffness of steel materials sharply deteriorate at high elevated temperatures. Consequently, the failure load of a tubular joint at high elevated temperature could be significantly smaller than its joint resistance at ambient temperature, which could cause progressive or sudden collapse of the entire structure. Recent years have seen a significant increase in the structural applications of high strength steel (HSS) due to their superior strength-to-weight ratio. The recent growths in manufacturing and metallurgical sectors facilitated the production of HSS with reduced carbon content and improved toughness. HSS of S960 and S1100 steel grades are used in the Fast Bridge 48 designed for the Swedish army. The bridge has a span of 46 m and is designed for a 65 ton tank for more than 1000 crossings [3]. The structural applications of HSS are comprehensively detailed in Pandey and Young [4]. The high strengths combined with natural stiff form of hollow section members enable the construction of stronger and lighter structures. However, the lack of adequate research work and design recommendations are the primary reasons hampering the widespread use of high strength structural steels. In addition, some challenges also need to be addressed in order to implement large scale structural applications of HSS, including welding of HSS, high notch sensitivity of HSS, softening in the heat affected region of HSS, preheating of thin HSS material for welding, use of current ultimate deformation limit ($0.03b_0$), high cost-to-material ratio, fatigue of HSS and so on.

It should be noted that a series of experimental investigations [4-9] on cold-formed S900 and S960 steel grades T- and X-joints were conducted by the authors. In addition, Pandey et al. [1,10] proposed design rules for predicting the static strengths of cold-formed S900 and S960 steel grades T- and TF-joints. Moreover, experimental and numerical investigations on box-section T- and X-joints with steel grades ranging from S460 to S960 were conducted by Lan et al. [11,12]. It is worth noting that these studies [1,4-12] were performed at ambient temperature, and no investigation is currently available on the static performance of HSS tubular joints at elevated temperatures (*T*). So far, all investigations on the static behaviour of hollow section joints at elevated temperatures were conducted on normal strength steel (i.e. steel grade less than and equal to S460) joints with main focus on CHS joints.

In this study, elevated temperature joint resistances ($N_{f,T}$) of cold-formed high strength steel square and rectangular hollow section (SHS and RHS) 90° T-joints were numerically investigated. The $N_{f,T}$ of cold-formed high strength steel (CFHSS) SHS and RHS (henceforth, RHS include SHS) T-joints undergoing compression loads were numerically studied at four elevated temperatures, including 400°C, 500°C, 600°C and 1000°C. It should be stressed that design rules for predicting the resistances of tubular joints at elevated temperatures are not given in international codes and guides. As a result, in this study, economical and reliable design rules are proposed by modifying the design equations proposed by Pandey et al. [1] for CFHSS RHS 90° T-joints at ambient temperature. Moreover, the applicability of current design rules given in EC3 [13] and CIDECT [14] using mechanical properties at elevated temperatures was also examined. Overall, it is shown that, on using the mechanical properties at elevated temperatures, the current design rules given in EC3 [13] and CIDECT [14] are uneconomical and unreliable. In addition, the predictions from design rules given in EC3 [13] and CIDECT [14] are quite dispersed.

2. Review of investigations conducted on tubular joints at elevated temperatures

Chen et al. [15] studied the static performance of CHS T-joints with ring stiffeners at elevated temperatures and finally proposed design equations for predicting the residual resistances of the investigated joints. Using transient state analysis, Gao et al. [16] studied the structural behaviour of CHS T-joints with collar plates. The residual resistances of concrete-filled CHS T-joints after fire exposures were studied by Gao et al. [17]. The influence of critical geometric parameters on the residual resistances of CHS T-joints at elevated temperatures was studied by Cheng et al. [18]. Lan and Huang [19] numerically investigated the joint resistances of duplex, austenitic and AISI 304 stainless steel RHS T- and X-joints at elevated temperatures and proposed design equations for their ultimate resistances. Feng and Young [20] carried out a numerical investigation on duplex and AISI 304 stainless steel RHS T- and X-joints using mechanical properties proposed by Chen and Young [21] at elevated temperatures. Subsequently, design rules were proposed by applying temperature correction factors on design equations given in CIDECT [14]. Nassiraei et al. [22] proposed design equations for CHS X-joints at elevated temperatures, where specimens were reinforced with collar plates. Two methods for predicting the ultimate capacities of CHS T-joints at elevated temperatures were proposed by Shao et al. [23] by duly investigating the effects of critical geometric parameters. Using non-linear regression analysis, Dodaran et al. [24] proposed a design formula to predict the resistances of KT-joints at elevated temperatures. Lan et al. [25] numerically studied the static performance of duplex, austenitic and AISI 304 stainless steel RHS K- and N-joints at elevated temperatures. In addition, design rules were also proposed by Lan et al. [25] using residual yield strengths.

The residual joint resistances of CHS T-joints subjected to brace in-plane bending load were investigated by Fung et al. [26] at elevated temperatures. Static performance of CHS T-joint without internal stiffeners was studied by Tan et al. [27] using experimental and numerical methods. It was reported that the joint resistance sharply reduced at high temperatures. The critical temperature of CHS K-joints was determined using the deformation rate based criterion in He et al. [28]. Compression loaded full-scale CHS T-joints were experimentally and numerically studied at elevated temperatures by Nguyen et al. [29,30]. The residual resistances of impacted CHS T-joints at elevated temperatures were investigated by Yu et al. [31]. The post-fire residual capacities of CHS T-joints were experimentally studied by Jin et al. [32]. Liu et al. [33] performed a numerical parametric study to investigate the static behaviour of CHS T-joints at elevated temperatures. The structural performance of CHS T-joints subjected to blast and fire was experimentally studied by Yu et al. [34]. The technique of artificial neural network was used by Xu et al. [35] to estimate the resistances of CHS T-joints at elevated temperatures. Ozyurt et al. [36] numerically investigated the joint resistances of CHS and SHS T-, Y-, X-, K- and N-joints at elevated temperatures. Based on numerical results, reduction factors were proposed to estimate the residual resistances of the investigated joints. Ozyurt et al. [37] numerically investigated the joint resistances of elliptical hollow section (EHS) T-and X-joints at elevated temperatures.

3. Approach used in this investigation

The numerical investigation was conducted using ABAQUS [38]. In the absence of any experimental investigation on CFHSS RHS T-joints at elevated temperatures, the numerical investigation in this study was performed using the finite element (FE) models developed and validated by Pandey et al. [1] for cold-formed S900 and S960 steel grades RHS 90° T-joints at ambient temperature. It is important to note that similar FE models were successfully used by Pandey and Young [2] to validate the test results of fire exposed (i.e. post-fire) cold-formed S900 and S960 steel grades RHS 90° T-joints using post-fire mechanical properties. As natural fires have different temperature vs time curves and also due to substantial cost involved in a fire test, numerical studies are popularly used for such investigations. It is due to these reasons, the FE models of tubular joints validated against ambient temperature test results were used in many numerical studies [19,20,25,36,37,39-51] for their corresponding elevated temperatures investigations.

The numerical investigation in this study was performed using the constitutive stress-strain model proposed by Li and Young [52] for S900 steel grade tubular members at elevated temperatures. The tubular members used in Pandey et al. [1], Pandey and Young [2] and Li and Young [52,53] were produced by the identical manufacturer and had similar chemical compositions, therefore, the constitutive stress-strain model proposed by Li and Young [52] at elevated temperatures can safely be used in this study. The numerical investigation was then performed using the mechanical properties predicted from stress-strain model [52] at 400°C, 500°C, 600°C and 1000°C. It should be noted that coupon specimens were extracted from the flat regions of tubular members. The stress-strain curves of cold-formed S900 steel grade tubular member obtained using steady state tests for temperatures ranging from 100°C to 1000°C are reported in Li and Young [53]. It should be noted that for temperatures less than 400°C, the deterioration of mechanical properties of cold-formed S900 steel grade tubular member was insignificant. As reported in Li and Young [53], the residual values of ultimate strength of cold-formed S900 steel grade tubular member at 400°C, 500°C, 600°C and 1000°C were 83%, 60%, 35% and 2% of the corresponding ultimate strength at ambient temperature.

Therefore, in order to investigate a wide range of strength reductions at elevated temperatures, the numerical investigation in this study was performed at 400°C, 500°C, 600°C and 1000°C.

4. Outline of test programs carried out on cold-formed high strength steel RHS T-joints at ambient temperature and post-fire conditions

At ambient temperature, the static performance of cold-formed S900 and S960 steel grades RHS 90° T-joints was experimentally investigated by Pandey and Young [54]. The braces and chords were welded using robotic metal active gas welding. In total, twenty-four 90° T-joint tests were conducted, where simply supported test specimens were axially compressed via braces. The nominal 0.2% proof stresses of tubular members were 900 and 960 MPa. The symbols b, h, t and R stand for cross-section width, depth, thickness and external corner radius of RHS member, respectively. The subscripts of symbols 0 and 1 denote chord and brace, respectively. Fig. 1 presents various notations for RHS T-joints. The failure modes identified in the tests [54] were chord face failure (F), chord side wall failure (S) and a combination of these two failure modes, named combined failure (F+S). The lengths of braces (L_1) were equal to two times the maximum of brace cross-section width (b_1) and depth (h_1). On the other hand, the lengths of chords (L_0) were equal to h_1 + 3h_0 +180 mm. The test results were obtained in the form of N vs u and N vs v curves, where N, u and v stand for static brace axial compression load, chord face indentation and chord side wall deformation, respectively.

The static behaviour of cold-formed steel fire exposed RHS 90° T-joints of S900 and S960 grades was investigated by Pandey and Young [55]. Before conducting the static joint tests, the test specimens were subjected to a total of three fire exposures with preselected post-fire peak temperatures (ψ) equal to 300°C, 550°C and 750°C, respectively. In total, sixteen 90° T-joints were tested under compression loads with simply supported chords. The nominal 0.2% proof stresses of without fire exposed tubular members were 900 and 960 MPa. The braces and chords were welded using robotic metal active gas welding. The test specimens were exposed to fire inside a gas furnace, where the furnace temperature was increased in accordance with the ISO-834 [56]. After attaining the preselected post-fire peak temperatures (ψ), the test specimens were allowed to naturally cool inside the furnace. Subsequently, at ambient temperature, RHS 90° T-joint test specimens were axially compressed through brace members.

5. Numerical programs on cold-formed high strength steel RHS T-joints at ambient temperature and post-fire conditions

5.1. General

The numerical investigations on cold-formed steel RHS 90° T-joints of S900 and S960 grades at ambient temperature and post-fire conditions were conducted by Pandey et al. [1] and Pandey and Young [2], respectively. The static (general) analysis procedure given in ABAQUS [38] was used as the solver. The isotropic strain hardening law was selected for the analysis, while the yielding onsets of FE models were based on the von-Mises yield theory. In the FE analyses, the growth of the time step was kept non-linear in order to reduce the overall computation time. Furthermore, the default Newton-Raphson method was used to find the roots of non-linear equilibrium equations. The material non-linearities were considered in the FE models developed for ambient temperature and post-fire conditions by assigning the measured values of ambient temperature and post-fire static stress-strain values of flat and corner portions of RHS members. However, experimentally obtained constitutive material curves both at ambient temperature and post-fire conditions were transformed into true stress-strain curves prior to their inclusion into the FE models. The true stress (σ_{true}) and true plastic strain ($\varepsilon_{true,pl}$) were determined in accordance with ABAQUS [38], where $\sigma_{true} = \sigma\,(1+\varepsilon)$ and $\varepsilon_{true,pl} = \ln\,(1+\varepsilon) - \sigma_{true}\,/E_o$. The terms σ and ε are the measured stress and strain obtained from tensile coupon tests, respectively. It is important to input the engineering stress-strain data as true stress and true plastic strain so that numerical analysis can correlate the current deformed state of the material with the history of previously deformed states and not with the initial undeformed state. In other words, true stress (σ_{true}) and true plastic strain ($\varepsilon_{true,pl}$) are used for the accurate definition of plastic behaviour of ductile materials. On the other hand, the geometric non-linearities in both ambient temperature and post-fire FE models were considered by enabling the non-linear geometry parameter (*NLGEOM) in ABAQUS [38]. The labelling of both ambient temperature and post-fire FE specimens was kept identical to the label system used in their corresponding test programs [54,55]. Fig. 2 presents typical FE RHS T-joints modelled for ambient temperature investigation [1], which also remain valid for corresponding post-fire numerical investigation [2].

5.2. Mesh spacing, element type and mechanical properties

Excluding welds, all other parts of both ambient temperature and post-fire FE models [1,2] were developed using the C3D20 elements. On the other hand, the C3D10 elements were used to model the weld parts due to their complicated shapes. The weld parts were freely meshed using the free-mesh algorithm, however, brace and chord parts were meshed using the structure-mesh algorithm. The use of solid elements helped in making realistic fusions between tubular and weld parts of FE models. Convergence studies were conducted using different mesh sizes, and finally, chord and brace members were seeded at spacing of 4 mm and 7 mm, respectively. Moreover, the seeding spacings of weld parts reciprocated the seeding spacings of their respective brace parts. In order to ensure the smooth transfer of stresses from flange to web regions, the corner portions of RHS were split into ten elements. FE analyses were also conducted to examine the influence of divisions along the wall thickness (t) of RHS members. The results of these FE analyses demonstrated the trivial influence of wall thickness divisions on the load vs deformation curves of the investigated RHS T-joints. The use of the C3D20 element as well as the small thickness of test specimens [54,55] led to such observations. It is worth noting that similar findings were also obtained in other studies [1,10,57]. Thus, for the validations of both ambient temperature and post-fire FE models, the wall thickness of tubular members was not divided. The measured values of ambient temperature and post-fire static stress-strain curves of flat and corner portions of RHS members [54,58] were used in the corresponding FE models. In addition, the influence of cold-working was included in the FE models by assigning wider corner regions. Various distances for corner extension were considered in the sensitivity analyses, and finally, the corner portions were extended by $2t$ into the neighbouring flat portions, which was in agreement with other studies conducted on CFHSS tubular members and joints [1,2,10,59-61].

5.3. Contact interactions and weld modelling

The RHS T-joint test specimens in the ambient and post-fire investigation [54,55] were welded using automatic gas metal arc welding process. An FD-B4L series of robot from OTC Daihen was employed for the welding process. The brace and chord members of RHS T-joints were tack-welded initially after being carefully aligned using the measured dimensions of the tubular members. The tubular joints were then mounted on the automatic rotating chuck whose rotation was synchronized with the movements of the robotic arm. The entire welding operation was controlled by an experienced and certified welder. An active gas mixture comprising 80% Ar and 20% CO_2 at 15 to 20 litres per minute was used for the shielding of fresh weld deposits during the course of the welding operation. Also, during the welding operation, the T-joint junction to welding nozzle distance varied between 10 to 15 mm. The welds were designed in accordance with the prequalified tubular joint details given in AWS D1.1M [62]. A low alloy solid carbon steel wire of diameter 1.2 mm, conforming to ER120S-G class of AWS A5.28M [63], was used as the filler material. The tensile material properties of the filler material used during the course of welding operation were also determined by fabricating and testing filler material coupons [64]. The measured average static 0.2% proof stress, tensile strength and elongation at the fracture of the filler material was 965.2 MPa, 1023.4 MPa and 17.2%, respectively. For more detailed information, regarding the fabrication and test results of filler material coupons, reference can be made to Pandey and Young [64].

In order to avoid excessive heat input, and thus, any further damage to tubular members near the brace-chord junction region, the weld leg size and numbers of weld passes were kept minimum to satisfy their respective design criteria. During the welding process, adopted values of the arc voltage, current and weld deposition speed were 16 V, 150 A and 300 mm/min, respectively. These inputs for welding operation were carefully selected after several trials of welding in order to achieve the desired weld leg sizes, weld shapes and to control the heat input during welding process. Using these weld inputs, the calculated value of the heat input was 0.384 kJ/mm. The welds were modelled in both ambient temperature and post-fire FE models using the average values of measured weld sizes reported in test programs [54,55]. The fillet weld was modelled for FE specimens when $\beta \leq 0.80$, where β is equal to b_1/b_0. However, when $\beta > 0.80$, fillet and groove welds (FW and GW) were modelled along the chord face and chord side directions, respectively. The inclusions of weld geometries appreciably improved the overall accuracies of FE models. In addition, modelling of weld parts helped attain realistic load transfer between brace and chord members.

A total of two types of contact interactions was defined in the FE models. First, contact interaction between brace and chord members of the FE models. Second, contact interaction between chord members and bearing blocks. In addition, a tie constraint was also established between weld and tubular members of the FE models. Both contact interactions were established using the built-in surface-to-surface contact definition. The contact interaction between brace and chord members of FE models was kept frictionless, while a frictional penalty equal to 0.3 was imposed on the contact interaction between chord member and bearing blocks. Along the normal direction of these two contact interactions, a 'hard' contact pressure overclosure was used. In addition, finite sliding was permitted between the interaction surfaces. For contact interactions and tie constraint, the surfaces were connected to each other using the 'master-slave' algorithm technique. This technique permits the separation of fused surfaces under tension, however, it does not allow penetration of fused surfaces under compression.

5.4. Boundary conditions and load application

In order to apply boundary conditions, three reference points were created in each T-joint FE model, including one top reference point (TRP) and two bottom reference points (BRP-1 and BRP-2), as shown in Fig. 2. The TRP replicated the fixed boundary condition of the top brace end, while BRP-1 and BRP-2 replicated the boundary conditions of the roller positioned at each chord end. The TRP was created at the cross-section centre of the top brace end, while BRP-1 and BRP-2 were created at 20 mm below the centre of the bottom surfaces of bearing blocks, which was in accordance with the test setup [54,55]. The TRP, BRP-1 and BRP-2 were then coupled to their corresponding surfaces using the built-in kinematic coupling type. In order to exactly replicate the boundary conditions of the T-joint test setup, all degrees of freedom (DOF) of TRP were restrained. On the other hand, for BRP-1 and BRP-2, except for the translations along the vertical and longitudinal directions of the T-joint FE specimen as well as the rotation about the transverse direction of the chord member, all other DOF of BRP-1 and BRP-2 were also restrained. In addition, all DOF of other nodes of T-joint FE specimen were kept unrestrained for both rotation and translation. Using the displacement control method, equal compression loads were then applied at the BRP-1 and -2 of FE models.

5.5. Geometric imperfection in chord webs

Garifullin et al. [65] studied the influence of geometric imperfections on the static behaviour of cold-formed steel hollow section T-joints. The imperfection profiles of RHS T-joints were obtained by performing elastic buckling analyses in ABAQUS [38]. It was concluded by Garifullin et al. [65] that geometric imperfections had a trivial influence on the static behaviour of hollow section T-joints. However, Pandey et al. [1] reported that the maximum measured values of cross-section width and depth of RHS members were on an average 2.9% more than their respective nominal dimensions. Therefore, it was necessary to model this geometric imperfection as an outward bulging 3-point convex arc, as shown in Fig. 3. Also, as all failure modes in tests [54,55] and numerical investigations [1,2] were only governed by the deformation of chord members, therefore, Pandey et al. [1] numerically examined the influence of outward bulging of chord cross-section on the static behaviour of RHS T-joints. Finally, it was concluded that the effect of convex bulging of chord cross-section was only significant for equal-width (i.e. β=1.0) RHS T-joints [1]. As a result, in both ambient temperature and post-fire FE models [1,2], geometric imperfections were introduced as a 3-point convex arc in the chord webs of equal-width RHS T-joints.

5.6. Validations of RHS T-joint FE models at ambient temperature and post-fire conditions

Both ambient temperature and post-fire FE models of cold-formed steel RHS 90° T-joints of S960 grade [1,2] were developed using the modelling techniques described in the preceding sub-sections of this paper. The validations of FE models were confirmed by duly comparing the joint resistances, load vs deformation curves and failure modes between tests [54,55] and corresponding FE [1,2] specimens. The measured dimensions of tubular members and welds were used to develop all FE models. In addition, measured ambient temperature and post-fire static mechanical properties of flat and corner portions of cold-formed S960 steel grade tubular members were used in the validations of corresponding ambient temperature and post-fire FE models. It is worth mentioning that for both ambient temperature and post-fire investigations, the peak load or 3% deformation limit load, whichever occurred earlier in the N vs u curve, was taken as the joint resistance [14]. For the ambient temperature investigation of cold-formed S960 steel grade RHS T-joints, the overall values of the mean (P_m) and coefficients of variation (COV) (V_p) of the comparisons between test and FE resistances were 1.00 and 0.014, respectively [1]. Besides, on using the similar FE models with post-fire static mechanical properties, the overall values of P_m and V_p of comparisons between post-fire test and FE resistances were 1.00 and 0.012, respectively [2]. In addition, the comparisons of load vs deformation curves between test and FE RHS T-joint specimens for ambient temperature and post-fire investigations are shown in Figs. 4 and 5, respectively. Furthermore, Figs. 6 and 7 present comparisons of distinct failure modes between typical test and FE RHS T-joint specimens for ambient temperature and post-fire investigations, respectively. Hence, it can be concluded that the verified FE models precisely replicated the overall static behaviour of cold-formed steel RHS 90° T-joints of S960 grade for both ambient temperature and post-fire investigations [1,2].

6. Numerical program of cold-formed high strength steel RHS T-joints at elevated temperatures

6.1. Parametric study

In the parametric study, the static behaviour of RHS 90° T-joints was investigated at 400°C, 500°C, 600°C and 1000°C. The FE analyses of parametric specimens were performed using mechanical properties at elevated temperatures predicted from the constitutive material model proposed by Li and Young [52] for cold-formed S900 steel grade tubular members. Fig. 8 presents the stress-strain curves at 400°C, 500°C, 600°C and 1000°C. Table 1 presents the mechanical properties at 400°C, 500°C, 600°C and 1000°C, which include Young's modulus (E_0), 0.2% proof stress ($\sigma_{0.2}$), ultimate strength (σ_u) and ultimate strain (ε_u). With the exception of mechanical properties at elevated temperatures, all FE modelling techniques described in Section 5 of this paper were used to perform the numerical parametric study on cold-formed S900 steel grade RHS T-joints at elevated temperatures. In total, 756 RHS 90° T-joint FE specimens were analysed in the parametric study, including 189 FE specimens corresponding to each elevated temperature. The validity ranges of governing geometric parameters were purposefully widened beyond the present limitations set by EC3 [13] and CIDECT [14]. Table 2 presents the overall ranges of various critical parameters considered in this investigation. In the parametric study, the values of cross-section width and depth of braces and chords of FE specimens varied from 30 mm to 600 mm, while the wall thickness of braces and chords varied from 2.25 mm to 12.5 mm. The external corner radii of braces and chords (R_1 and R_0) conformed to commercially produced HSS members [66]. In this study, R_1 and R_0 were kept as $2t$ for $t \leq 6$ mm, $2.5t$ for $6 < t \leq 10$ mm and $3t$ for $t > 10$ mm, which in turn also met the limits detailed in EN [67]. The lengths of braces (L_1) and chords (L_0) of RHS T-joint FE specimens were determined using the identical formulae used for the test specimens [54,55].

For meshing along the longitudinal and transverse directions of RHS members, seedings were approximately spaced at the minimum of $b/30$ and $h/30$. Overall, the adopted mesh sizes of parametric FE specimens varied from 3 to 12 mm. On the other hand, the seeding interval of weld parts of parametric FE specimens reciprocated the seeding interval of their corresponding brace parts. For precise replication of RHS curvatures, the corner portions of RHS members were split into ten parts. For RHS members with $t \leq 6$ mm, no divisions were made along the wall thickness of the parametric FE specimens. However, for RHS members with $t > 6$ mm, the wall thickness of parametric FE specimens was divided into two layers. With regard to the weld modelling, FW was modelled for FE specimens with $\beta \leq 0.80$. However, for FE specimens with $\beta > 0.80$, GW and FW were respectively modelled along the chord side and chord face directions. Following the prequalified tubular joint details given in AWS D1.1M [62], the leg size of FW was designed as 1.5 times the minimum of t_1 and t_0. In addition, referring to the prequalified tubular joint details given in AWS D1.1M [62], the weld reinforcement of GW was taken as half of the minimum wall thickness of brace and chord member. The designs of both FW and GW were consistent with the numerical investigations performed at ambient temperature and post-fire conditions [1,2]. The weld parts were also assigned the mechanical properties determined from the constitutive material model proposed by Li and Young [52]. In addition, as shown in Fig. 3, the flat part of each chord web (i.e. h_0-$2R_0$) of equal-width RHS T-joint was outward bulged at its centre by $0.015b_0$. Fig. 9 presents the stress nephograms of typical RHS T-joints failed by F, F+S and S modes.

6.2. Failure modes identified at elevated temperatures

Overall, three types of failure modes were identified in this numerical investigation. First, failure of RHS T-joints by chord flange yielding, which was termed as chord face failure and denoted by the letter ‘F’ in this study. Second, failure of RHS T-joints due to buckling of chord webs, which was termed as chord side wall failure and denoted by the letter ‘S’ in this study. Third, failure of RHS T-joints due to the combination of chord face and chord side wall failures, which was named as combined failure and denoted by ‘F+S’ in this study. The RHS T-joints were failed by the F mode, when the $N_{f,T}$ was determined using the $0.03b_0$ limit criterion. The applied load of RHS T-joint failed by the F mode was monotonically increasing. In this investigation, RHS T-joints were failed by the F mode when $0.30 \leq \beta \leq 0.75$. On the other hand, RHS T-joints were failed by the S mode when β=1.0. For RHS T-joints that failed by the F+S mode, the $N_{f,T}$ vs u curve exhibited a clear ultimate load. Additionally, evident deformations of chord flange, chord webs and chord corner regions were noticed in the specimens that failed by the F+S mode. The specimens were failed by the F+S mode in this investigation when $0.80 \leq \beta \leq 0.90$. Figs. 10 to 12 respectively present the variations of $N_{f,T}$ vs u curves for typical RHS T-joints that failed by the F, F+S and S failure modes.

7. Design rules

Currently, design rules for predicting the residual strengths of tubular joints at elevated temperatures are not given in international codes and guides. In order to examine the suitability of EC3 [13] and CIDECT [14] design provisions for cold-formed S900 steel grade RHS T-joints at elevated temperatures, in this study, the nominal resistances from design equations given in EC3 [13] and CIDECT [14] ($N_{E,T}$ and $N_{C,T}$) were determined using the mechanical properties shown in Table 1. The design rules given in EC3 [13] and CIDECT [14] are shown below:

Chord face failure ($\beta \leq 0.85$)

EC3 [13]:

$$N_{E,T} = C_f \left[k_n \frac{f_{y0,T} t_0^2}{(1-\beta)\sin\theta_1} \left(\frac{2\eta}{\sin\theta_1} + 4\sqrt{1-\beta} \right) / \gamma_{M5} \right] \tag{1}$$

CIDECT [14]:

$$N_{C,T} = C_f \left[Q_f \frac{f_{y0,T} t_0^2}{\sin\theta_1} \left(\frac{2\eta}{(1-\beta)\sin\theta_1} + \frac{4}{\sqrt{1-\beta}} \right) \right] \tag{2}$$

Chord side wall failure ($\beta = 1.0$)

EC3 [13]:

$$N_{E,T} = C_f \left[k_n \frac{f_{b,T} t_0}{\sin\theta_1} \left(\frac{2h_1}{\sin\theta_1} + 10t_0 \right) / \gamma_{M5} \right] \tag{3}$$

CIDECT [14]:

$$N_{C,T} = C_f \left[Q_f \frac{f_{k,T} t_0}{\sin\theta_1} \left(\frac{2h_1}{\sin\theta_1} + 10t_0 \right) \right] \tag{4}$$

The nominal resistances from EC3 [13] were determined using the 0.2% proof stress at elevated temperatures and partial safety factor (γ_{M5}) equal to 1.0. In addition, a material factor (C_f) equal to 0.80 was adopted as per EC3 [68]. On the other hand, CIDECT [14] uses the minimum of 0.2% proof stress and 0.80 times the corresponding ultimate strength for joint resistance calculation. Moreover, design provisions given in CIDECT [14] recommend the use of C_f equal to 0.90 for tubular joints with steel grade exceeding S355 and up to S460. Unlike EC3 [13], CIDECT [14] uses different values of partial safety factors (γ_M) for different tubular joints and their corresponding failure modes, which are given in IIW [69]. However, their effects have already been implicitly included inside the CIDECT [14] design provisions. Referring to IIW [69], the value of partial safety factor (γ_M) for RHS T-joints failed by both chord face failure and chord side wall failure modes is equal to 1.0. Thus, nominal resistances from CIDECT [14] were calculated using γ_M equal to 1.0 for both chord face failure and chord side wall failure modes. In Eqs. (1) to (4), chord stress functions are denoted by k_n and Q_f, yield stress of chord member at elevated temperatures is denoted by $f_{y0,T}$, the parameter η is equal to h_1/b_0, chord side wall buckling stresses at elevated temperatures are denoted by $f_{b,T}$ and $f_{k,T}$, and the angle between brace and chord is denoted by θ_1 (in degrees).

In addition, a reliability analysis was performed as per AISI S100 [70]. In this study, the design equation was treated as reliable when the value of the reliability index (β_0) was greater than or equal to 2.50. The values of various statistical parameters and load combinations used in the reliability index calculation are identical to those values adopted in Pandey et al. [1].

8. Comparisons of joint resistances at elevated temperatures with nominal resistances

For different observed failure modes, the overall summary of comparisons between $N_{f,T}$ and nominal resistances predicted from design rules given in EC3 [13] and CIDECT [14] using mechanical properties at elevated temperatures are shown in Tables 3 to 5. The comparisons are also graphically shown in Figs. 13 to 15 for different failure modes. Table 3 and Fig. 13 present comparisons for RHS T-joint specimens that failed by the F mode. The comparison results proved that using the mechanical properties at elevated temperatures, the design rules given in EC3 [13] and CIDECT [14] are very conservative but scattered and unreliable for the design of cold-formed S900 steel grade RHS T-joints at elevated temperatures. In Fig. 13, generally, RHS T-joint specimens with small values of β and η ratios and large values of 2γ ratio (b_0/t_0) lie below the unit slope line (i.e. y=x). For such specimens, the joint resistance corresponding to the $0.03b_0$ limit was not sufficient to cause the yielding of chord flanges. On the contrary, the yield line theory has been used to derive the existing design equation for RHS T-joint specimens that failed by the F mode [13,14]. Consequently, $N_{f,T}$ of RHS T-joint specimens became smaller than the corresponding nominal resistances predicted from design rules given in EC3 [13] and CIDECT [14] using mechanical properties at elevated temperatures. As a result, such cases fall below the line of unit slope. The data above the line of unit slope, on the other hand, indicate RHS T-joint specimens with medium to large values of β and η ratios and small values of 2γ ratio.

The comparison results of RHS T-joint specimens that failed by the F+S mode at elevated temperatures are shown in Table 4 and Fig. 14. It can be noticed that using mechanical properties at elevated temperatures, the current design provisions given in EC3 [13] and CIDECT [14] are found to be largely conservative but quite dispersed and unreliable. The data above the unit slope line in Fig. 14 typically represent RHS T-joints with large values of β ratio and small values of 2γ and h_0/t_0 ratios. As the β ratio of RHS T-joint failed by the F+S mode increased, the brace member gradually approached the chord corner regions. Consequently, the $N_{f,T}$ of such joints increased due to enhanced rigidity of the chord corner regions. On the other hand, the corresponding increase in nominal resistances predicted from design rules given in EC3 [13] and CIDECT [14] was lower than the $N_{f,T}$ of RHS T-joints. Subsequently, such data fall above the line of unit slope in Fig. 14. Table 5 and Fig.

15 present the comparison results of RHS T-joint specimens that failed by the S mode. The existing design rules, using mechanical properties at elevated temperatures, apparently provided very conservative predictions and were accompanied by significantly large values of COV. The EC3 [13] and CIDECT [14] design provisions for the S failure mode considered chord webs as pin-ended columns, which resulted in very conservative predictions as h_0/t_0 ratio increased.

9. Proposed design rules

Using two design approaches, named as proposal-1 and -2, design rules are proposed in this study for different failure modes of the investigated cold-formed steel RHS 90° T-joints of S900 grade at elevated temperatures (T). The design rules proposed in both the approaches (i.e. proposal-1 and -2) were based on the design equations proposed by Pandey et al. [1] for CFHSS RHS T-joints at ambient temperature. In the first design approach (i.e. proposal-1), mechanical properties at ambient temperature used in the design equations proposed by Pandey et al. [1] are replaced with the mechanical properties at elevated temperatures. In addition, a correction factor (Ω) based on the elevated temperature is also applied on the proposed design rules. On the other hand, in the second design approach (i.e. proposal-2), only a correction factor based on the elevated temperature is applied on the design rules proposed by Pandey et al. [1] at ambient temperature. It should be noted that the design rules proposed in this study are valid for 400°C ≤ T ≤ 1000°C and included angle (θ_1) equal to 90°. In order to obtain design resistances (N_d), the proposed nominal resistances (N_{pn1} and N_{pn2}) in the following sub-sections of this paper shall be multiplied by their correspondingly recommended resistance factors (ϕ), i.e. $N_d = \phi\ (N_{pn1}$ or $N_{pn2})$.

9.1. RHS T-joints failed by F mode at elevated temperatures ($0.30 \le \beta \le 0.75$)

Proposal-1:

Using mechanical properties at elevated temperatures (T):

$$N_{pn1} = \left(0.67e^{0.0009T}\right)\left[f_{y0,T}t_0^2\left(\frac{30\beta + 4.5\eta - 6.6}{0.5 + 0.03(2\gamma)}\right)\right] \tag{5}$$

Proposal-2:

Using mechanical properties at ambient temperature and elevated temperature correction factor (Ω):

$$N_{pn2} = \Omega \left[f_{y0} t_0^2 \left(\frac{30\beta + 4.5\eta - 6.6}{0.5 + 0.03(2\gamma)} \right) \right] \tag{6}$$

where

$$\Omega = \begin{bmatrix} 1.58 - 2\times10^{-3}T & \text{for} \quad 400°\text{C} \le T \le 600°\text{C} \\ 0.9 - 8.67\times10^{-4}T & \text{for} \quad 600°\text{C} < T \le 1000°\text{C} \end{bmatrix} \tag{7}$$

The Eqs. (5) and (6) are valid for $0.30 \le \beta \le 0.75$, $16.6 \le 2\gamma \le 50$, $16.6 \le h_0/t_0 \le 50$, $0.3 \le \eta \le 1.2$ and $0.75 \le \tau \le 1.0$. As shown in Table 3, the P_m and V_p of proposal-1 (i.e. Eq. (5)) are 1.01 and 0.201, respectively, while the P_m and V_p of proposal-2 (i.e. Eq. (6)) are 1.02 and 0.199, respectively. For Eqs. (5) and (6), ϕ equal to 0.75 is recommended, resulting in β_0 equal to 2.51 and 2.54, respectively. Thus, Eqs. (5) and (6) must be multiplied by ϕ equal to 0.75 to obtain their corresponding design resistances (N_d), respectively. The comparisons of $N_{f,T}$ of RHS T-joint specimens with nominal resistances predicted from design equations given in EC3 [13], CIDECT [14] as well as predictions from proposal-1 and -2 are graphically presented in Fig. 13.

9.2. RHS T-joints failed by F+S mode at elevated temperatures ($0.80 \le \beta \le 0.90$)

<u>Proposal-1:</u>

Using mechanical properties at elevated temperatures (T):

$$N_{pn1} = \left(0.6e^{0.0009T}\right) \left[f_{y0,T} t_0^2 \left(\frac{55\beta + 4.5\eta - 33}{0.75 + 0.0075(2\gamma)} \right) \right] \tag{8}$$

<u>Proposal-2:</u>

Using mechanical properties at ambient temperature and elevated temperature correction factor (Ω):

$$N_{pn2} = \Omega \left[f_{y0} t_0^2 \left(\frac{55\beta + 4.5\eta - 33}{0.75 + 0.0075(2\gamma)} \right) \right] \tag{9}$$

where

$$\Omega = \begin{bmatrix} 1.55 - 2\times10^{-3}T & \text{for} \quad 400°\text{C} \le T \le 600°\text{C} \\ 0.83 - 8\times10^{-4}T & \text{for} \quad 600°\text{C} < T \le 1000°\text{C} \end{bmatrix} \tag{10}$$

The Eqs. (8) and (9) are valid for $0.80 \le \beta \le 0.90$, $16.6 \le 2\gamma \le 50$, $16.6 \le h_0/t_0 \le 50$, $0.6 \le \eta \le 1.2$ and $0.75 \le \tau \le 1.0$. As shown in Table 4, the P_m and V_p of proposal-1 (i.e. Eq. (8)) are 1.00 and 0.150, respectively, while the P_m and V_p of proposal-2 (i.e. Eq. (9)) are 0.97 and 0.144, respectively. For Eqs. (8) and (9), ϕ equal to 0.80 and 0.75 are recommended, resulting in β_0 equal to 2.51 and 2.63, respectively. Thus, Eqs. (8) and (9) must be multiplied by ϕ equal to 0.80 and 0.75 to obtain their corresponding design resistances (N_d), respectively. The comparisons of $N_{f,T}$ of RHS T-joint specimens with nominal resistances predicted from design equations given in EC3 [13], CIDECT [14] as well as predictions from proposal-1 and -2 are graphically presented in Fig. 14.

9.3. RHS T-joints failed by S mode at elevated temperatures (β = 1.0)

<u>Proposal-1:</u>

Using mechanical properties at elevated temperatures (T):

$$N_{pn1} = \begin{cases} N_1 = (1.29 - 0.0008T)\left[\dfrac{f_{k,T}(2b_w t_0)}{(1.5\eta+1)}\left(\dfrac{1.83-0.05(2\gamma)+1.2\tau}{588\left(\dfrac{h_0}{t_0}\right)^{-2.17}}\right)\right] & \text{for} \quad 400°\text{C} \le T \le 600°\text{C} \\ N_2 = 12.74\left(\dfrac{h_0}{t_0}\right)^{-0.95}\left[\dfrac{f_{k,T}(2b_w t_0)}{(1.5\eta+1)}\left(\dfrac{1.83-0.05(2\gamma)+1.2\tau}{588\left(\dfrac{h_0}{t_0}\right)^{-2.17}}\right)\right] & \text{for} \quad T = 1000°\text{C} \\ \text{Linear interpolation between } N_1 \text{ and } N_2 & \text{for} \quad 600°\text{C} < T < 1000°\text{C} \end{cases} \tag{11}$$

<u>Proposal-2:</u>

Using mechanical properties at ambient temperature and elevated temperature correction factor (Ω):

$$N_{pn2} = \Omega\left[\frac{f_k(2b_w t_0)}{(1.5\eta+1)}\left(\frac{1.83-0.05(2\gamma)+1.2\tau}{588\left(\frac{h_0}{t_0}\right)^{-2.17}}\right)\right] \tag{12}$$

where

$$\Omega = \begin{cases} 1.77 - 2.3\times10^{-3}T & \text{for} \quad 400°\text{C} \le T \le 600°\text{C} \\ 0.945 - 9.2\times10^{-4}T & \text{for} \quad 600°\text{C} < T \le 1000°\text{C} \end{cases} \tag{13}$$

The Eqs. (11) and (12) are valid for β = 1.0, $16.6 \le 2\gamma \le 50$, $10 \le h_0/t_0 \le 60$, $0.6 \le \eta \le 1.2$ and $0.75 \le \tau \le 1.25$. As shown in Table 5, the P_m and V_p of proposal-1 (i.e. Eq. (11)) are 1.01 and 0.200, respectively, while the P_m and V_p of proposal-2 (i.e. Eq. (12)) are 1.03 and 0.200, respectively. For Eqs. (11) and (12), ϕ equal to 0.75 is recommended, resulting in β_0 equal to 2.52 and 2.57, respectively. Thus, Eqs. (11) and (12) must be multiplied by ϕ equal to 0.75 to obtain their corresponding design resistances (N_d), respectively. The comparisons of $N_{f,T}$ of RHS T-joint specimens with nominal resistances predicted from design equations given in EC3 [13], CIDECT [14] as well as predictions from proposal-1 and -2 are graphically presented in Fig. 15. The buckling curve 'a' of EC3 [71] was used to determine the $f_{k,T}$ and f_k in Eqs. (11) and (12). Moreover, the flat portions of chord side walls were equal to h_0-2R_0. Additionally, instead of assuming pin-ended boundary conditions for the flat portions of chord side walls, the effective length of the chord side wall column was determined using a factor equal to 0.85. Therefore, in this study, the effective lengths of the flat portions of chord side walls were equal to 0.85×(h_0-2R_0). The definition of the width of the chord web column (b_w) was identical to that given in EC3 [13] and CIDECT [14].

It is important to note that for RHS T-joint specimens with $0.75 < \beta < 0.80$ and $0.90 < \beta < 1.0$, the nominal resistances under proposal-1 can be obtained by performing a linear interpolation between Eqs. (5) & (8) and Eqs. (8) & (11), respectively. Similarly, for proposal-2, the nominal resistances of RHS T-joint specimens with $0.75 < \beta < 0.80$ and $0.90 < \beta < 1.0$ can be obtained by performing a linear interpolation between Eqs. (6) & (9) and Eqs. (9) & (12), respectively.

10. Conclusions

A numerical program has been conducted in this study with an aim to investigate the static performance of cold-formed steel 90° T-joints of S900 grade with square and rectangular hollow section (SHS and RHS) braces and chords at elevated temperatures (T). The resistances of simply supported RHS 90° T-joints undergoing brace axial compression loads were determined at 400°C, 500°C, 600°C and 1000°C. The numerical investigation was performed through the finite element (FE) method using the constitutive stress-strain model proposed by Li and Young [52] for cold-formed S900 steel grade tubular members at elevated temperatures. A total of 756 FE 90° RHS T-joint specimens were analysed in the parametric study, where the validity ranges of important geometric parameters exceeded the limits prescribed in EC3 [13] and CIDECT [14]. The welds were modelled in all RHS T-joint specimens. Overall, RHS T-joints were failed by three failure modes, including chord face failure (F), chord side wall failure (S), and a combination of these two failure modes, i.e. combined failure (F+S) mode. The nominal resistances predicted from design rules given in EC3 [13] and CIDECT [14], using mechanical properties at elevated temperatures, were compared with the resistances of RHS T-joints investigated in this study. Generally, it has been shown that the current design rules given in EC3 [13] and CIDECT [14] are uneconomical and unreliable for the investigated T-joints. Moreover, the predictions from design rules given in EC3 [13] and CIDECT [14] are quite dispersed. Consequently, for the design of cold-formed steel RHS 90° T-joints of S900 grade at elevated temperatures ranging from 400°C to 1000°C, economical and reliable design rules are proposed in this study using the two design approaches.

Acknowledgement

The work described in this paper was fully supported by a grant from the Research Grants Council of the Hong Kong Special Administrative Region, China (Project No. 17210218).

References

[1] Pandey M, Chung KF and Young B. Design of cold-formed high strength steel tubular T-joints under compression loads. Thin-Walled Structures, 2021;164:107573.

[2] Pandey M and Young B. Design of Cold-Formed High Strength Steel Rectangular Hollow Section T-Joints Subjected to Post-Fire Conditions, Journal of Constructional Steel Research (under review).

[3] Ma JL, Chan TM and Young B. Material properties and residual stresses of cold-formed high strength steel hollow sections. Journal of Constructional Steel Research, 2015;109:152-165.

[4] Pandey M and Young B. Structural performance of cold-formed high strength steel tubular X-Joints under brace axial compression. Engineering Structures, 2020; 208:109768.

[5] Pandey M and Young B. Static resistances of cold-formed high strength steel tubular non-90° X-Joints. Engineering Structures, 2021;239:112064.

[6] Pandey M and Young B. Ultimate Resistances of Member-Rotated Cold-Formed High Strength Steel Tubular T-Joints under Compression Loads, Engineering Structures, 2021;244:112601.

[7] Pandey M and Young B. Effect of Member Orientation on the Static Strengths of Cold-Formed High Strength Steel Tubular X-Joints, Thin-walled Structures, 2022;170:108501.

[8] Pandey M and Young B. Stress Concentration Factors of Cold-Formed High Strength Steel Tubular T-Joints, Thin-walled Structures, 2021;166:107996.

[9] Pandey M and Young B. Experimental Investigation on Stress Concentration Factors of Cold-formed High Strength Steel Tubular X-Joints, Engineering Structures, 2021;243:112408.

[10] Pandey M, Chung KF and Young B. Numerical investigation and design of fully chord supported tubular T-joints. Engineering Structures, 2021;239:112063.

[11] Lan X, Chan TM and Young B. Structural behaviour and design of high strength steel RHS X-joints. Engineering Structures, 2019; 200:109494.

[12] Lan X, Chan TM and Young B. Testing, finite element analysis and design of high strength steel RHS T-joints. Engineering Structures, 2021; 227:111184.

[13] Eurocode 3 (EC3), Design of Steel Structures-Part 1-8: Design of Joints, EN 1993-1-8, European Committee for Standardization, CEN, Brussels, Belgium, 2005.

[14] Packer JA, Wardenier J, Zhao XL, Vegte GJ van der, Kurobane Y. Design guide for rectangular hollow section (RHS) joints under predominantly static loading. Comite´ International pour le Developpement et l'Etude de la Construction TuECbulaire (CIDECT), Design Guide No. 3, 2nd edn., LSS Verlag, Dortmund, Germany, 2009.

[15] Chen C, Shao YB, Yang J. Study on fire resistance of circular hollow section (CHS) T-joint stiffened with internal rings, Thin-Walled Structures, 2015;92:104–114.

[16] Gao F, Guan XQ, Zhu HP, Liu XN. Fire resistance behaviour of tubular T-joints reinforced with collar plates, J. Constr. Steel Res. 2015; 115:106–120.

[17] Gao F, Zhu H, Liang H, Tian Y. Post-fire residual strength of steel tubular T-joint with concrete-filled chord, Journal of Constructional Steel Research, 2017; 139:327–338.

[18] Cheng C, Shao Y, Yang J. Experimental and numerical study on fire resistance of circular tubular T-joints, Journal of Constructional Steel Research, 2013; 85:24–39.

[19] Lan X and Huang Y. Structural design of cold-formed stainless steel tubular X-and T-joints at elevated temperatures. Thin-Walled Structures, 2016; 108:270-279.

[20] Feng R. and Young B. Design of cold-formed stainless steel tubular joints at elevated temperatures. Engineering Structures, 2012;35:188-202.

[21] Chen J, Young B. Stress-strain curves for stainless steel at elevated temperatures. Engineering Structures, 2006;28(2):229–39.

[22] Nassiraei H, Lotfollahi-Yaghin MA, Neshaei SA, Zhu L. Structural behavior of tubular X-joints

strengthened with collar plate under axially compressive load at elevated temperatures, Marine Structures, 61 (2018) 46–61.
[23] Shao Y, Haicheng Z, Dongping Y. Discussion on two methods for determining static strength of tubular T-joints at elevated temperature, Advances in Structural Engineering, 2017:20 (5):704–721.
[24] Dodaran NA, Ahmadi H, Lotfollahi-Yaghin MA. Static strength of axially loaded tubular KT-joints at elevated temperatures: study of geometrical effects and parametric formulation, Marine Structures, 2018; 61:282–308.
[25] Lan X, Huang Y, Chan TM and Young B. Static strength of stainless steel K-and N-joints at elevated temperatures. Thin-Walled Structures, 2018;122:501-509.
[26] Fung TC, Tan KH and Nguyen MP. Structural behavior of CHS T-joints subjected to static in-plane bending in fire conditions. Journal of Structural Engineering, 2016;142(3):04015155.
[27] Tan KH, Fung TC and Nguyen MP. Structural behavior of CHS T-Joints subjected to brace axial compression in fire conditions. Journal of Structural Engineering, 2013; 139(1):73-84.
[28] He S, Shao Y, Zhang H and Wang Q. Parametric study on performance of circular tubular K-joints at elevated temperature. Fire safety journal, 2015; 71:174-186.
[29] Nguyen MP, Fung TC and Tan KH. An experimental study of structural behaviours of CHS T-joints subjected to brace axial compression in fire condition. Tubular Structures XIII, Hong Kong, 2010:725-732.
[30] Nguyen MP, Tan KH and Fung TC. Numerical models and parametric study on ultimate strength of CHS T-joints subjected to brace axial compression under fire condition. Tubular Structures XIII, Hong Kong, 2010:733-740.
[31] Yu W, Zhao J, Luo H, Shi J and Zhang D. Experimental study on mechanical behavior of an impacted steel tubular T-joint in fire. Journal of Constructional Steel Research, 2011; 67(9):1376-1385.
[32] Jin M, Zhao J, Chang J and Zhang D. Experimental and parametric study on the post-fire behavior of tubular T-joint. Journal of Constructional Steel Research, 2012; 70:93-100.
[33] Liu M, Zhao J and Jin M. An experimental study of the mechanical behavior of steel planar tubular trusses in a fire. Journal of Constructional Steel Research, 2010; 66(4):504-511.
[34] Yu W, Zhao J, Luo H, Shi J and Zhang D. Experimental study on mechanical behavior of an impacted steel tubular T-joint in fire. Journal of Constructional Steel Research, 2011; 67(9):1376-1385.
[35] Xu J, Zhao J, Song Z and Liu M. Prediction of ultimate bearing capacity of Tubular T-joint under fire using artificial neural networks. Safety science, 2012; 50(7):1495-1501.
[36] Ozyurt E, Wang YC and Tan KH. Elevated temperature resistance of welded tubular joints under axial load in the brace member. Engineering Structures, 2014;59:574-586.
[37] Ozyurt E and Wang YC. Resistance of axially loaded T-and X-joints of elliptical hollow sections at elevated temperatures–a finite element study, Structures, 2018; 14:15-31.
[38] Abaqus/Standard. Version 6.17. USA: K. a. S. Hibbit; 2017.
[39] Ozyurt E and Wang YC. A numerical investigation of static resistance of welded planar steel tubular joints under in-plane and out-of-plane bending at elevated temperatures. Engineering Structures, 2019; 199:109622.
[40] Nassiraei H, Mojtahedi A, Lotfollahi-Yaghin MA and Zhu L. Capacity of tubular X-joints reinforced with collar plates under tensile brace loading at elevated temperatures. Thin-Walled Structures, 2019; 142:426-443.
[41] Azari-Dodaran N, Ahmadi H, Zhu L and Li P. Experimental and numerical study of the ultimate load for collar-plate-reinforced tubular K-joints at fire-induced elevated temperatures. Ships

and Offshore Structures, 2022;17(5):1159-1177.
[42] Ozyurt E. Finite element study on axially loaded reinforced Square Hollow Section T-joints at elevated temperatures. Thin-Walled Structures, 2020; 148:106582.
[43] Lan X, Wang F, Luo Z, Liu D, Ning C and Xu X. Joint strength reduction factor of internally ring-stiffened tubular joints at elevated temperatures. Advances in Structural Engineering, 2016; 19(10):1650-1660.
[44] Azari-Dodaran N and Ahmadi H. Numerical study on the ultimate load of offshore two-planar tubular KK-joints at fire-induced elevated temperatures. Journal of Marine Engineering & Technology, 2022;21(4):205-233.
[45] Dodaran NA, Ahmadi H and Lotfollahi-Yaghin MA. Parametric study on structural behavior of tubular K-joints under axial loading at fire-induced elevated temperatures. Thin-Walled Structures, 2018; 130:467-486.
[46] Ozyurt E and Wang YC. Resistance of T- and K-joints to tubular members at elevated temperatures. In Proc of Applications of Structural Fire Engineering, Wald, Burgess, Horova, Jana, Jirku (eds), CTU Publishing House, Prague, 2013:179-185.
[47] Ozyurt E and Wang YC. Resistance of welded tubular T-and X-joints made of high strength steel at elevated temperatures. In Proceedings of the 17th international symposium on tubular structures, 2019:9-12.
[48] Azari-Dodaran N and Ahmadi H. Static behavior of offshore two-planar tubular KT-joints under axial loading at fire-induced elevated temperatures. Journal of Ocean Engineering and Science, 2019; 4(4):352-372.
[49] Wang YC and Ozyurt E. Static resistance of axially loaded multiplanar gap KK-joints of Circular Hollow sections at elevated temperatures. Engineering Structures, 2021; 229:111676.
[50] Nassiraei H. Static strength of tubular T/Y-joints reinforced with collar plates at fire induced elevated temperature. Marine Structures, 2019; 67:102635.
[51] Azari-Dodaran N and Ahmadi H. Structural behavior of right-angle two-planar tubular TT-joints subjected to axial loadings at fire-induced elevated temperatures. Fire Safety Journal, 2019; 108:102849.
[52] Li HT and Young B. Cold-formed high strength steel SHS and RHS beams at elevated temperatures. Journal of Constructional Steel Research, 2019; 158:475-485.
[53] Li HT and Young B. Material properties of cold-formed high strength steel at elevated temperatures. Thin-Walled Structures, 2017; 115:289-299.
[54] Pandey M, Young B. Tests of cold-formed high strength steel tubular T-joints. Thin-Walled Structures, 2019;143:106200.
[55] Pandey M and Young B. Post-Fire Behaviour of Cold-Formed High Strength Steel Tubular T- and X-Joints, Journal of Constructional Steel Research, 2021;186:106859.
[56] ISO-834. Fire-resistance tests-Elements of Building Construction-Part 1-General requirements. ISO 834-1, International Organization of Standards, 1999.
[57] Crockett P. Finite element analysis of welded tubular connections. PhD Thesis, University of Nottingham, 1994.
[58] Pandey M, Young B. Post-fire Mechanical Response of High Strength Steels. Thin-Walled Structures, 2021;164:107606.
[59] Ma JL, Chan TM and Young B. Design of cold-formed high strength steel tubular beams. Engineering Structures, 2017;151:432-443.
[60] Li QY and Young B. Design of cold-formed steel built-up open section members under combined compression and bending. Thin-Walled Structures, 2022;172:108890.
[61] Li HT and Young B. Cold-formed stainless steel RHS members undergoing combined bending

and web crippling: Testing, modelling and design. Engineering Structures, 2022;250:113466.
[62] AWS D1.1/D1.1M, Structural Welding Code – Steel, American Welding Society (AWS), Miami, USA, 2020.
[63] AWS A5.28/A5.28M, Specification for Low-Alloy Steel Electrodes and Rods for Gas Shielded Arc Welding, American Welding Society (AWS), Miami, USA, 2015.
[64] Pandey M, Young B. Compression capacities of cold-formed high strength steel tubular T-joints. J Constr Steel Res, 162, 105650, 2019.
[65] Garifullin M, Bronzova MK, Heinisuo M, Mela K and Pajunen S. Cold-formed RHS T joints with initial geometrical imperfections. Magazine of Civil Engineering, 2018;82(6).
[66] SSAB. Strenx Tube 960 MH. Data Sheet 2043, Sweden, 2017.
[67] EN 10219-2. Cold formed welded structural hollow sections of non-alloy and fine grain steels-Part 2: Tolerances, dimensions and sectional properties. European Committee for Standardization (CEN), Brussels, Belgium; 2006.
[68] Eurocode 3 (EC3), Design of steel structures. Part 1-12: Additional rules for the extension of EN 1993 up to steel grades S700, EN 1993-1-12, European Committee for Standardization, CEN, Brussels, Belgium, 2007.
[69] IIW Doc. XV-1402-12 and IIW Doc. XV-E-12-433. Static design procedure for welded hollow section joints – Recommendations. International Institute of Welding, Paris, France, 2012.
[70] AISI S100. North American Specification for the design of cold-formed steel structural members. American Iron and Steel Institute (AISI), Washington, D.C., USA, 2016.
[71] Eurocode 3 (EC3), Design of Steel Structures–Part 1-1: General Rules and Rules for Buildings, EN 1993-1-1, European Committee for Standardization (CEN), Brussels, Belgium, 2005.

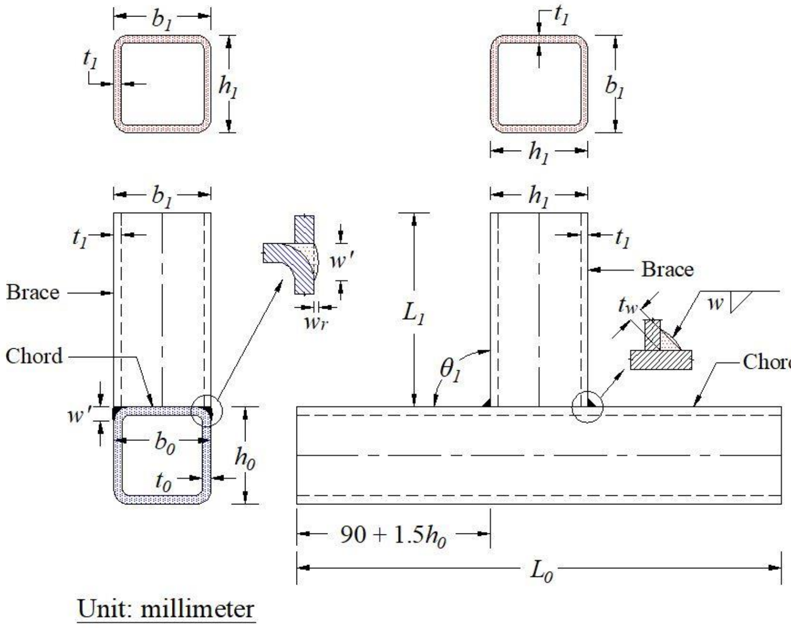

Fig. 1. Representation of geometric notations for RHS T-joint.

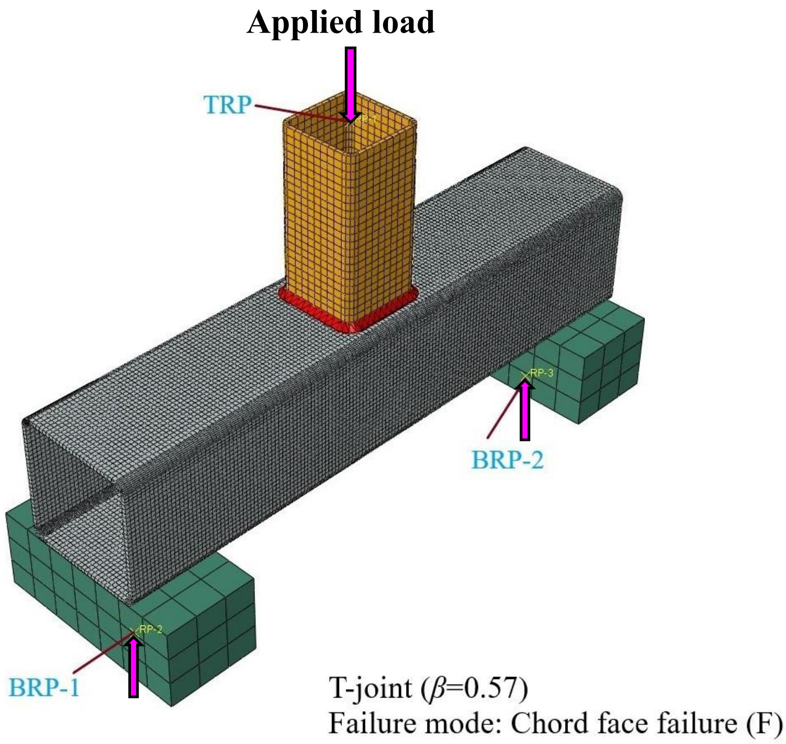

(a) 3D geometrical view of typical FE model of RHS T-joint with β=0.57.

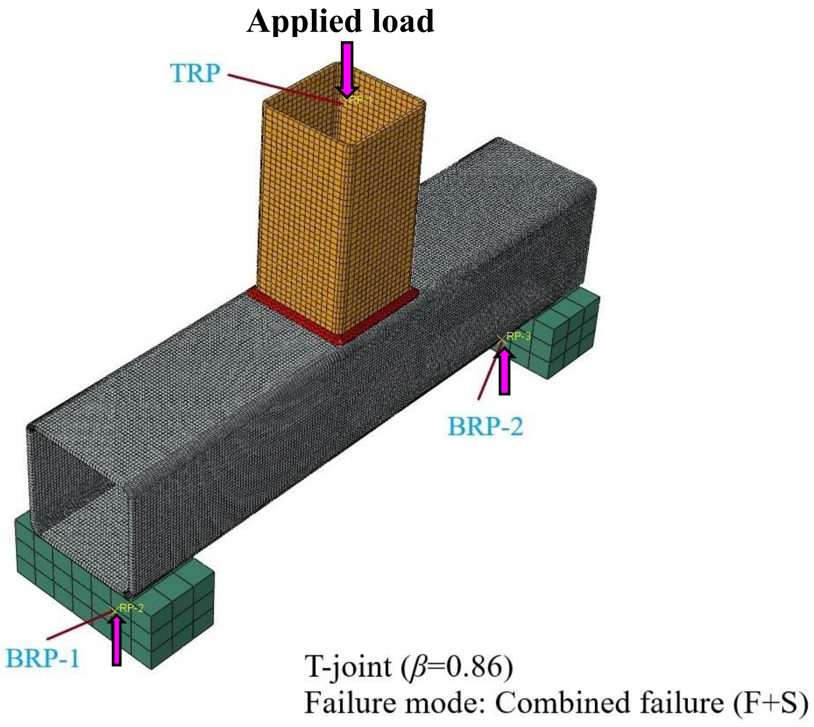

(b) 3D geometrical view of typical FE model of RHS T-joint with β=0.86.

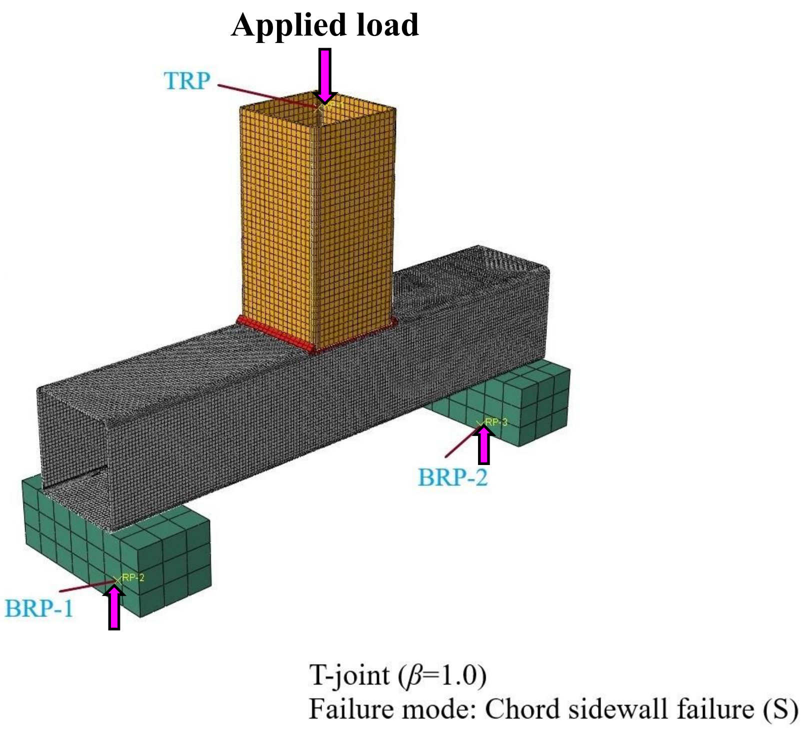

(c) 3D geometrical view of typical FE model of RHS T-joint with β=1.0.

Fig. 2. 3D geometrical views of typical FE models of RHS T-joints.

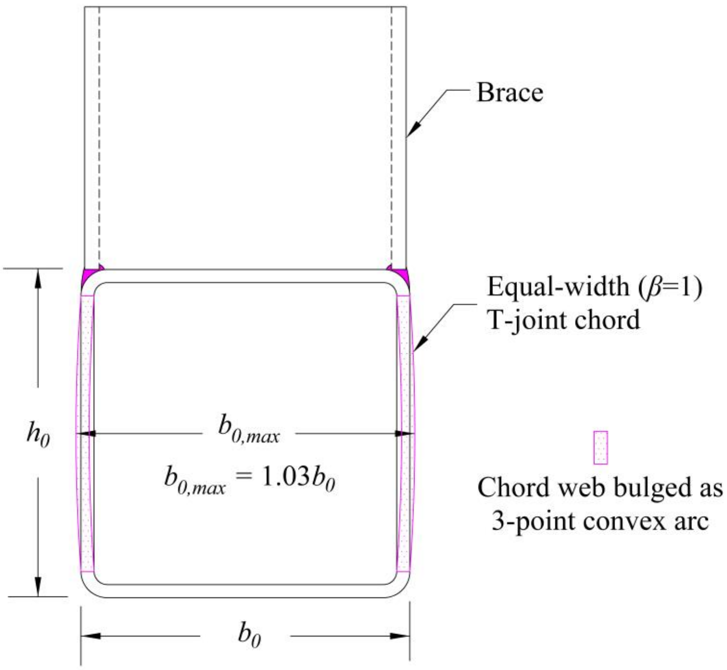

Fig. 3. Initial geometric imperfection modelled in chord webs of equal-width RHS T-joint.

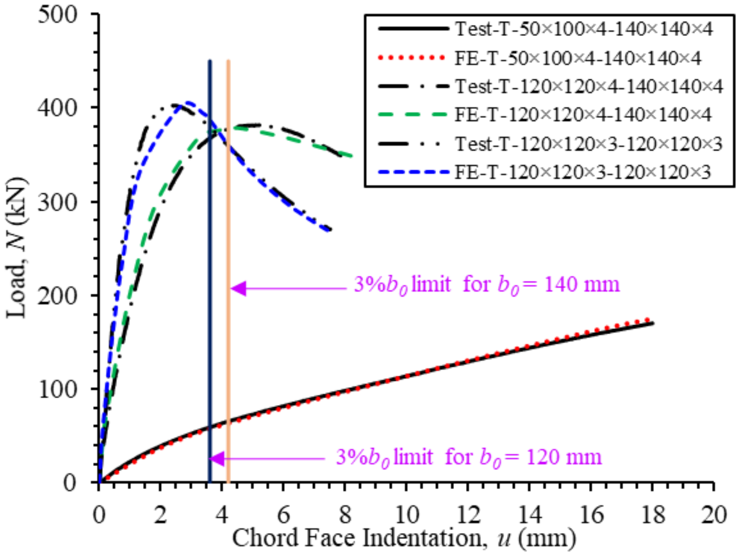

(a) Load vs chord face indentation curves.

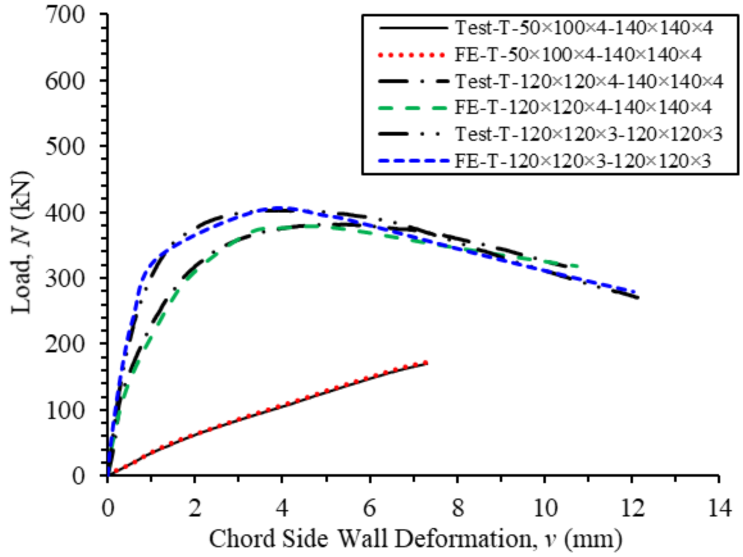

(b) Load vs chord side wall deformation curves.

Fig. 4. Test vs FE load-deformation curves for RHS T-joints at ambient temperature.

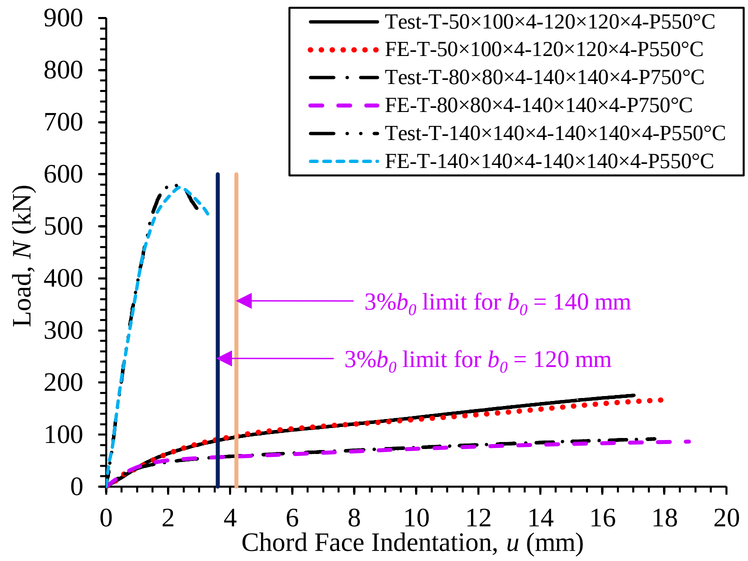

(a) Load vs chord face indentation curves.

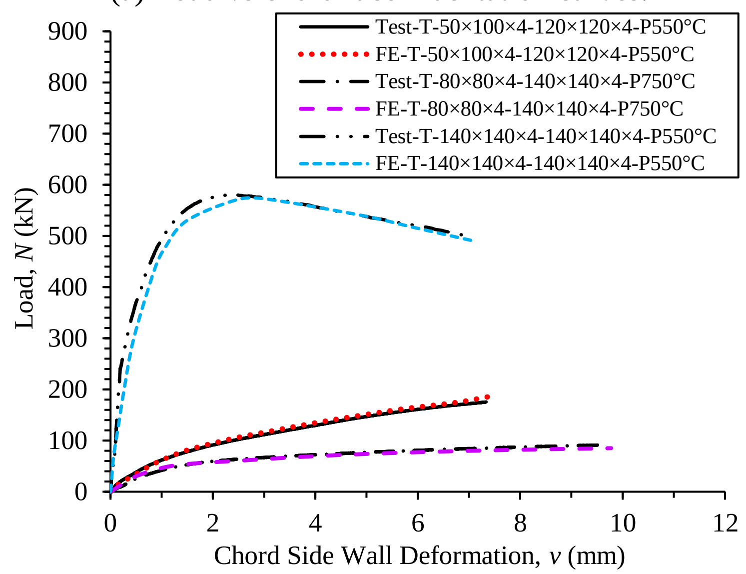

(b) Load vs chord side wall deformation curves.

Fig. 5. Test vs FE load-deformation curves for RHS T-joints for post-fire conditions.

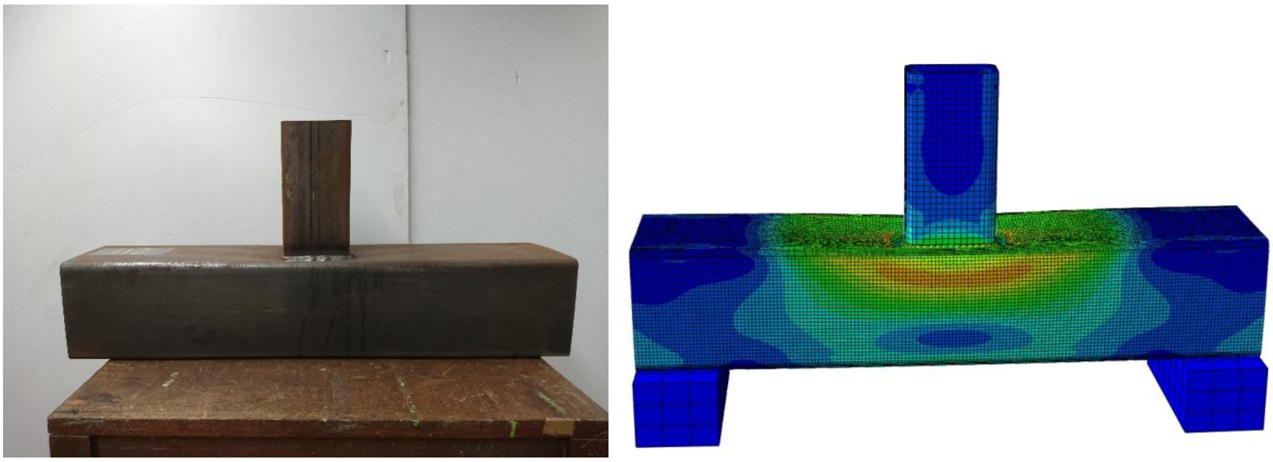

(a) Test vs FE comparison for RHS T-joint failed by F mode at ambient temperature.

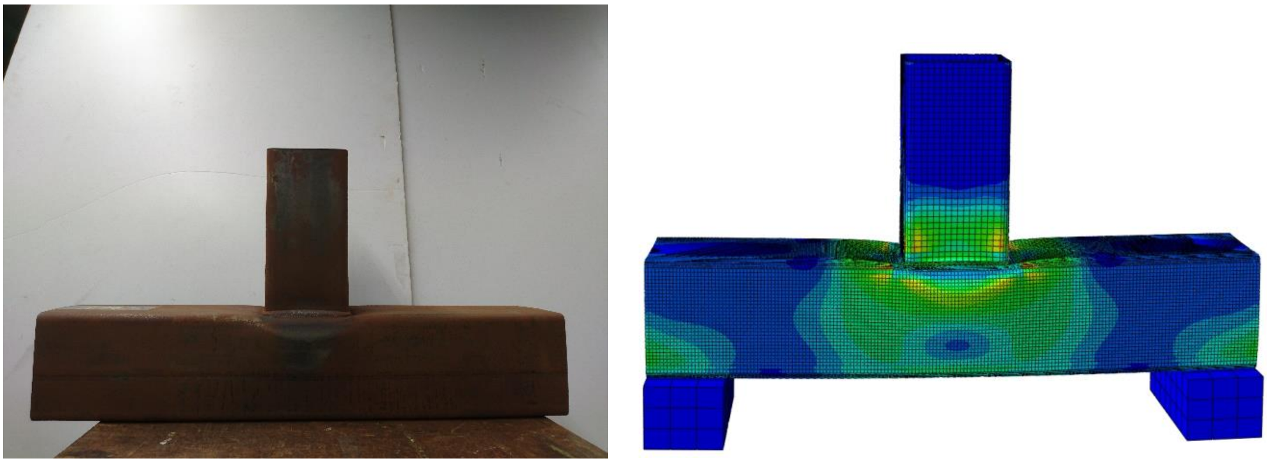

(b) Test vs FE comparison for RHS T-joint failed by F+S mode at ambient temperature.

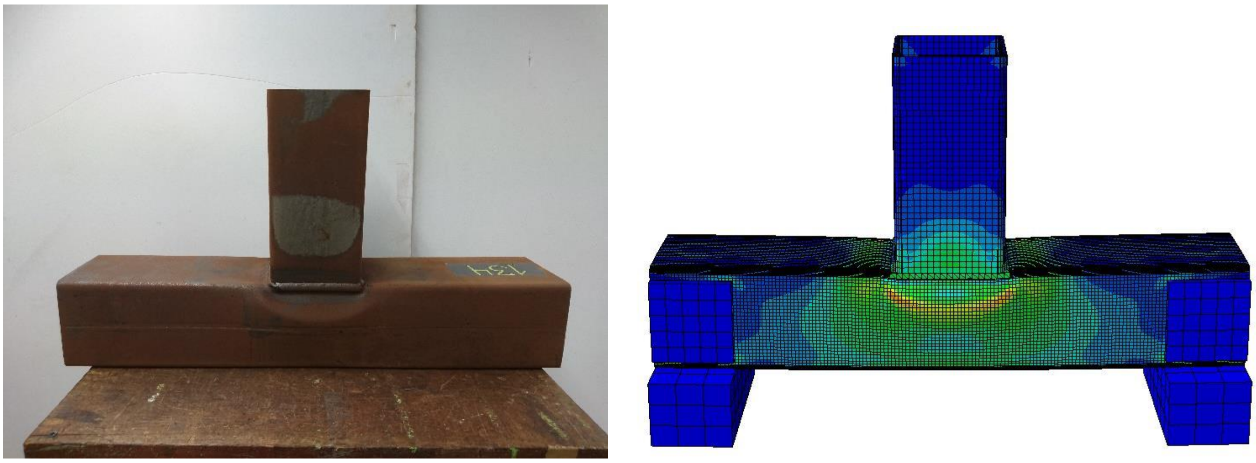

(c) Test vs FE comparison for RHS T-joint failed by S mode at ambient temperature.

Fig. 6. Test vs FE comparisons of failure modes for RHS T-joints at ambient temperature.

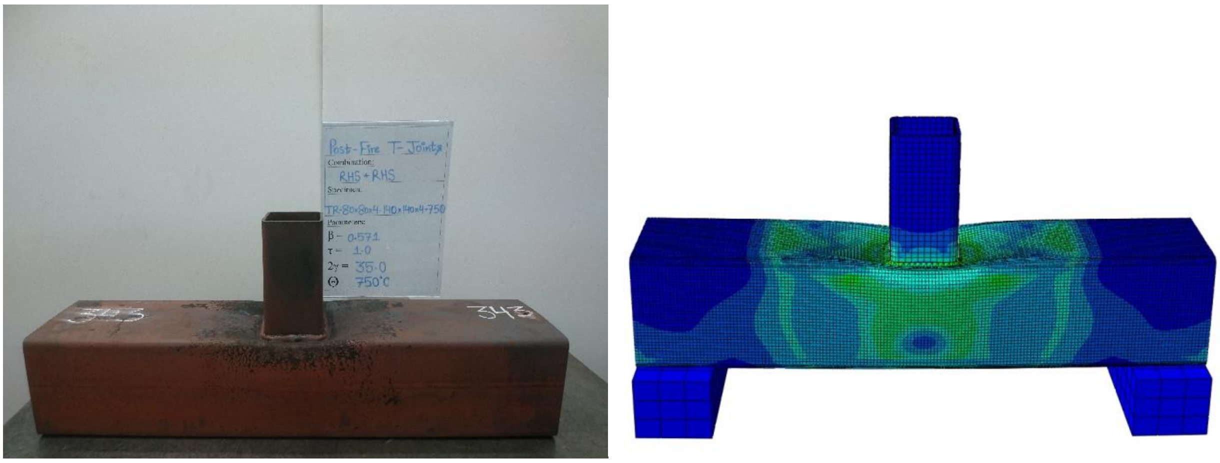

(a) Test vs FE comparison for RHS T-joint failed by F mode for post-fire condition.

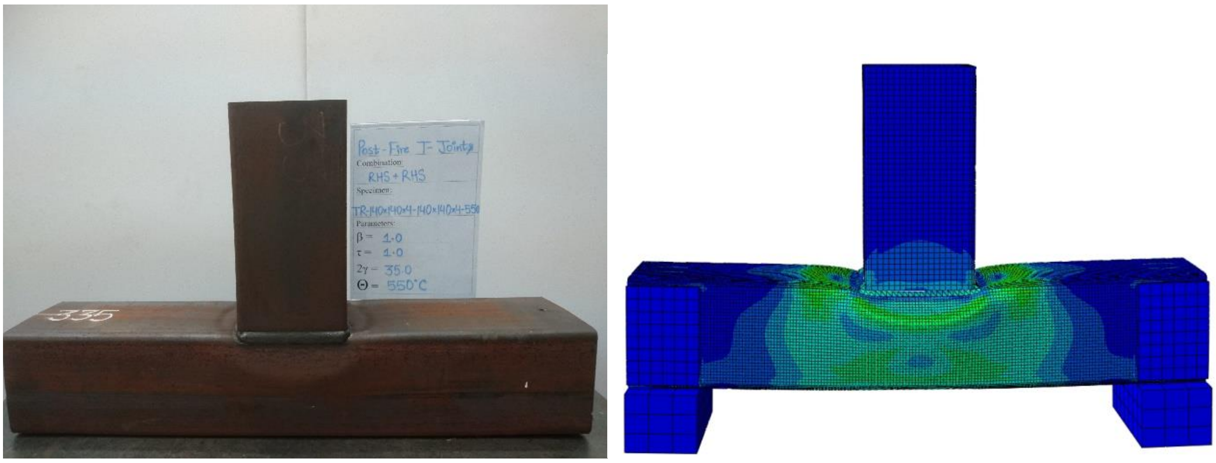

(b) Test vs FE comparison for RHS T-joint failed by S mode for post-fire condition.

Fig. 7. Test vs FE comparisons of failure modes for RHS T-joints for post-fire conditions.

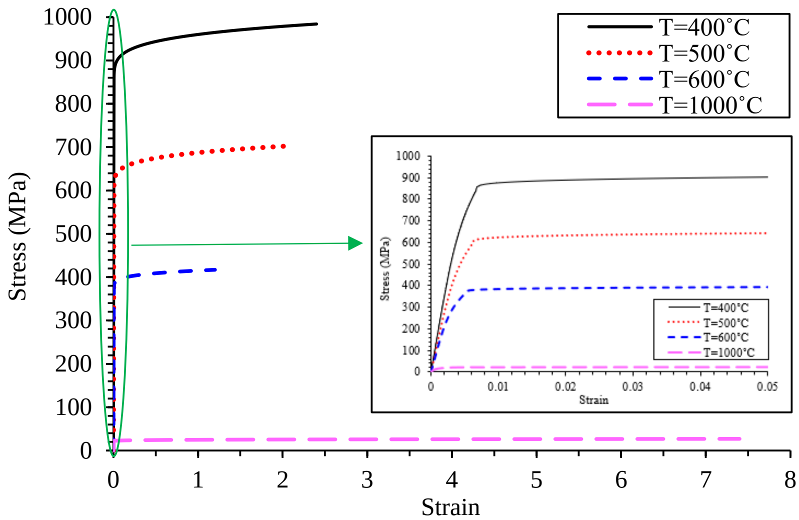

Fig. 8. Stress-strain curves used in parametric study at elevated temperatures [52].

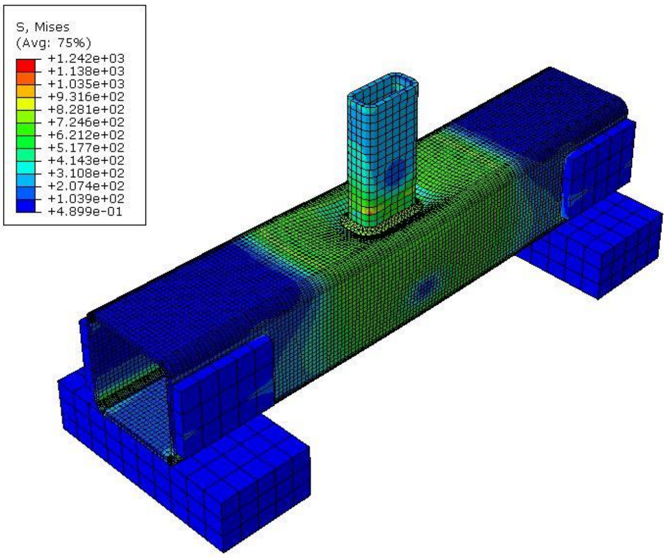

(a) Stress nephogram of RHS T-joint FE model failed by F mode.

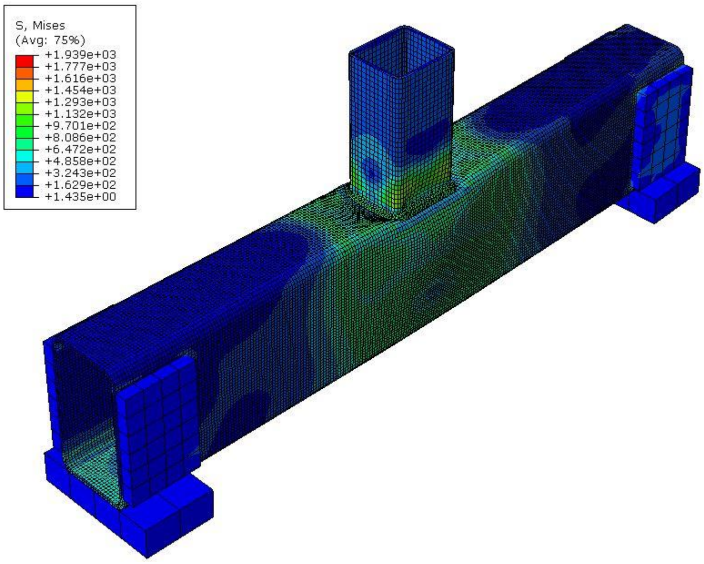

(b) Stress nephogram of RHS T-joint FE model failed by F+S mode.

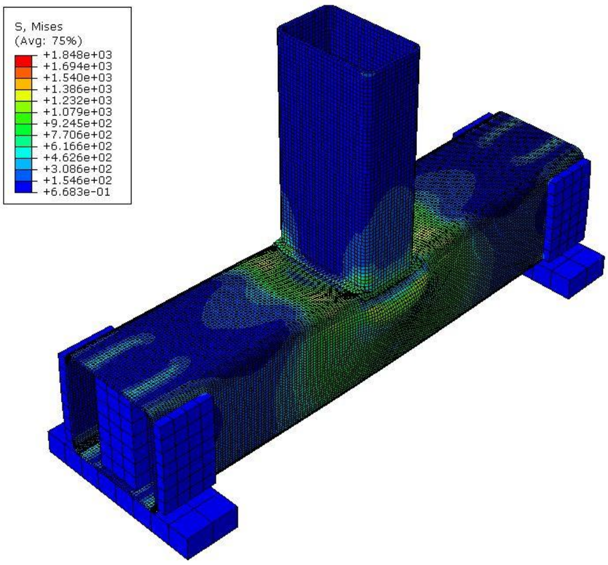

(c) Stress nephogram of RHS T-joint FE model failed by S mode.

Fig. 9 Stress nephograms of typical RHS T-joints at elevated temperatures.

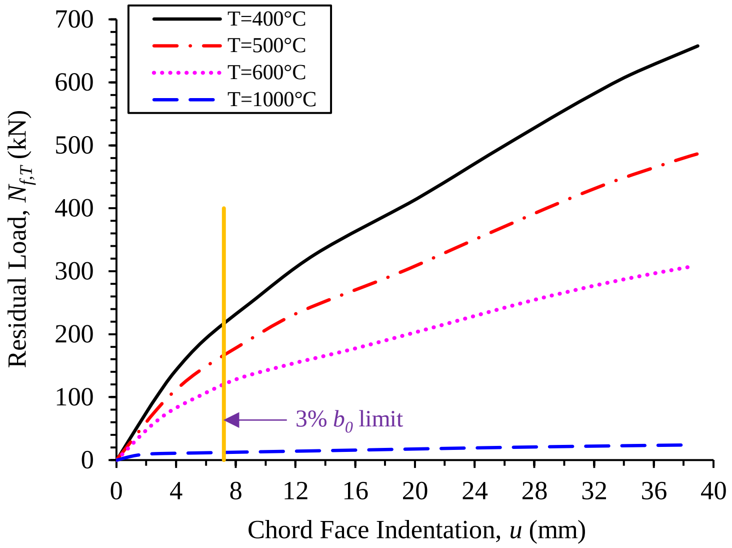

Fig. 10. Variations of load vs deformation curves for typical RHS T-joint (T-72×216×6-240×240×8; β=0.30) failed by F mode at elevated temperatures.

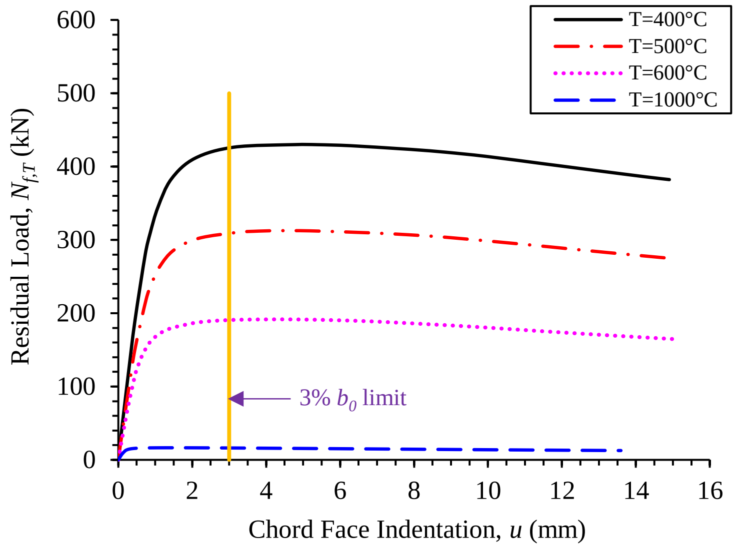

Fig. 11. Variations of load vs deformation curves for typical RHS T-joint (T-80×60×4.5-100×100×6; β=0.80) failed by F+S mode at elevated temperatures.

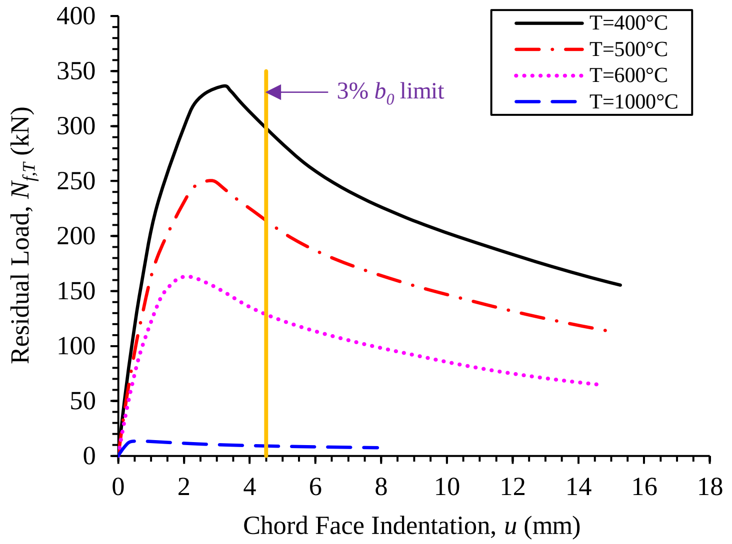

Fig. 12. Variations of load vs deformation curves for typical RHS T-joint (T-150×180×3.75-150×120×3; β=1.0) failed by S mode at elevated temperatures.

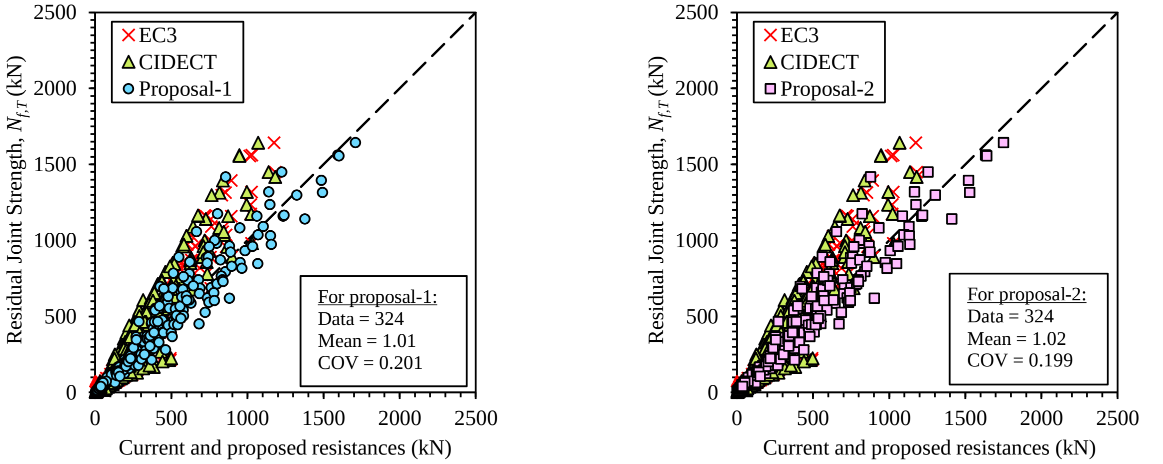

(a) For Proposal-1. (b) For Proposal-2.

Fig. 13. Comparisons of joint resistances at elevated temperatures with current and proposed nominal resistances for RHS T-joints failed by F mode.

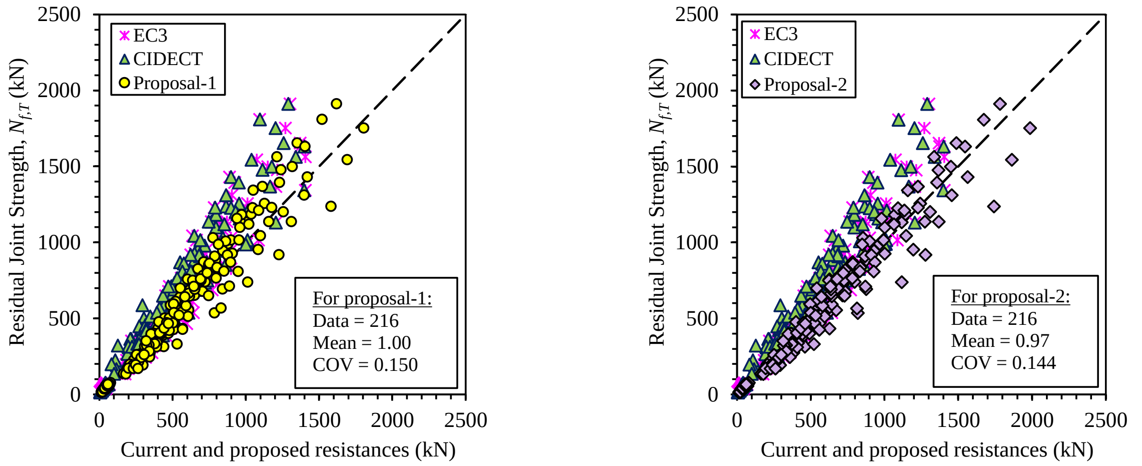

(a) For Proposal-1. (b) For Proposal-2.

Fig. 14. Comparisons of joint resistances at elevated temperatures with current and proposed nominal resistances for RHS T-joints failed by F+S mode.

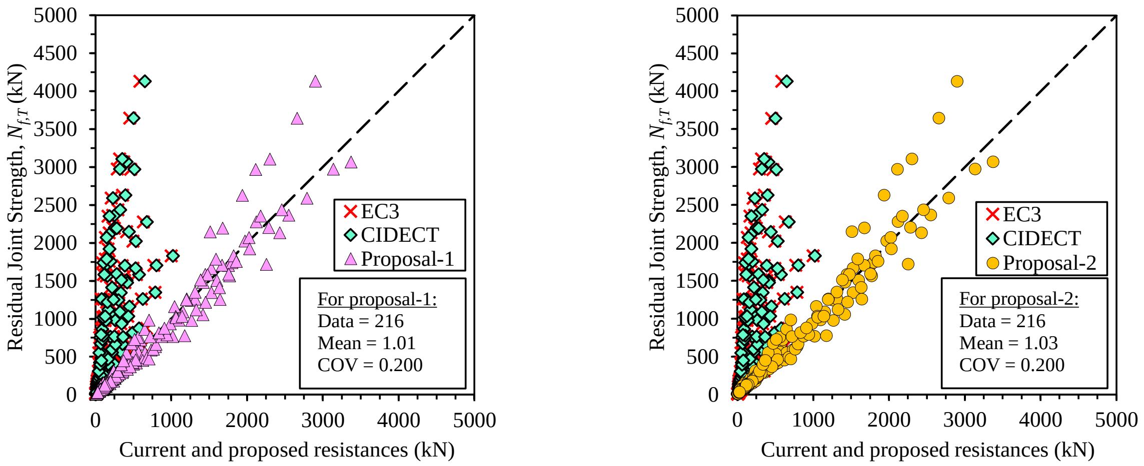

(a) For Proposal-1. (b) For Proposal-2.

Fig. 15. Comparisons of joint resistances at elevated temperatures with current and proposed nominal resistances for RHS T-joints failed by S mode.

Table 1. Mechanical properties at elevated temperatures [52].

Temperatures (°C)	Nominal Yield Strengths (MPa)	Mechanical properties at elevated temperatures				
		E_0 (GPa)	$\sigma_{0.2}$ (MPa)	σ_u (MPa)	$0.80\sigma_u$ (MPa)	ε_u (%)
21	900	207	1024	1181	945	2.4
400	900	179	839	984	787	2.4
500	900	143	594	703	562	2.1
600	900	114	368	417	334	1.2
1000	900	30	21	27	22	7.4

Table 2. Overall ranges of critical parameters used in parametric study.

Parameters	Validity Ranges
T	[400°C to 1000°C]
β (b_1/b_0)	[0.30 to 1.0]
2γ (b_0/t_0)	[16.6 to 50]
h_0/t_0	[10 to 60]
η (h_1/b_0)	[0.3 to 1.2]
τ (t_1/t_0)	[0.75 to 1.25]

Table 3. Summary of comparisons between joint resistances at elevated temperatures with existing and proposed nominal resistances for RHS T-joints failed by F mode.

Elevated Temperatures (T)	Parameters	Comparisons			
		$\frac{N_{f,T}}{N_{E,T}}$	$\frac{N_{f,T}}{N_{C,T}}$	$\frac{N_{f,T}}{N_{pn1}}$	$\frac{N_{f,T}}{N_{pn2}}$
400°C	No. of data (n)	81	81	81	81
	Mean (P_m)	1.08	1.18	1.04	1.02
	COV (V_p)	0.308	0.345	0.175	0.175
500°C	No. of data (n)	81	81	81	81
	Mean (P_m)	1.13	1.22	1.01	1.02
	COV (V_p)	0.310	0.338	0.187	0.187
600°C	No. of data (n)	81	81	81	81
	Mean (P_m)	1.05	1.22	0.96	1.01
	COV (V_p)	0.292	0.326	0.226	0.226
1000°C	No. of data (n)	81	81	81	81

	Mean (P_m)	1.48	1.70	1.03	1.02
	COV (V_p)	0.267	0.306	0.209	0.209
Overall	No. of data (n)	324	324	324	324
	Mean (P_m)	1.18	1.33	1.01	1.02
	Maximum	2.10	2.64	1.65	1.70
	Minimum	0.26	0.28	0.49	0.51
	COV (V_p)	0.327	0.364	0.201	0.199
	Resistance factor (ϕ)	1.00	1.00	0.75	0.75
	Reliability index (β_0)	1.55	1.80	2.51	2.54

Table 4. Summary of comparisons between joint resistances at elevated temperatures with existing and proposed nominal resistances for RHS T-joints failed by F+S mode.

Elevated Temperatures (T)	Parameters	Comparisons			
		$\frac{N_{f,T}}{N_{E,T}}$	$\frac{N_{f,T}}{N_{C,T}}$	$\frac{N_{f,T}}{N_{pn1}}$	$\frac{N_{f,T}}{N_{pn2}}$
400°C	No. of data (n)	54	54	54	54
	Mean (P_m)	1.17	1.32	1.06	0.96
	COV (V_p)	0.165	0.172	0.134	0.134
500°C	No. of data (n)	54	54	54	54
	Mean (P_m)	1.18	1.35	0.99	0.95
	COV (V_p)	0.171	0.206	0.140	0.140
600°C	No. of data (n)	54	54	54	54
	Mean (P_m)	1.09	1.30	0.93	0.96
	COV (V_p)	0.161	0.211	0.159	0.159
1000°C	No. of data (n)	54	54	54	54
	Mean (P_m)	1.49	1.72	1.01	0.99
	COV (V_p)	0.248	0.228	0.142	0.142
Overall	No. of data (n)	216	216	216	216
	Mean (P_m)	1.23	1.41	1.00	0.97
	Maximum	3.50	3.13	1.33	1.29
	Minimum	0.74	0.87	0.62	0.64
	COV (V_p)	0.235	0.240	0.150	0.144
	Resistance factor (ϕ)	1.00	1.00	0.80	0.75
	Reliability index (β_0)	1.97	2.46	2.51	2.63

Table 5. Summary of comparisons between joint resistances at elevated temperatures with existing and proposed nominal resistances for RHS T-joints failed by S mode.

Elevated Temperatures (T)	Parameters	Comparisons			
		$\frac{N_{f,T}}{N_{E,T}}$	$\frac{N_{f,T}}{N_{C,T}}$	$\frac{N_{f,T}}{N_{pn1}}$	$\frac{N_{f,T}}{N_{pn2}}$
400°C	No. of data (n)	54	54	54	54
	Mean (P_m)	5.72	6.03	1.02	0.98
	COV (V_p)	0.774	0.644	0.202	0.200
500°C	No. of data (n)	54	54	54	54
	Mean (P_m)	5.39	5.73	1.06	0.99
	COV (V_p)	0.775	0.634	0.206	0.197
600°C	No. of data (n)	54	54	54	54
	Mean (P_m)	3.99	4.40	0.97	0.97
	COV (V_p)	0.712	0.565	0.236	0.250
1000°C	No. of data (n)	54	54	54	54
	Mean (P_m)	2.01	2.35	1.00	1.18
	COV (V_p)	0.603	0.296	0.144	0.151
Overall	No. of data (n)	216	216	216	216
	Mean (P_m)	4.36	4.89	1.01	1.03
	Maximum	18.69	16.77	1.72	1.58
	Minimum	0.88	1.37	0.65	0.67
	COV (V_p)	0.856	0.687	0.200	0.200
	Resistance factor (ϕ)	1.00	1.00	0.75	0.75
	Reliability index (β_0)	2.17	2.84	2.52	2.57